Cutting of sheep carcass using 3D point cloud with dual-robot system

Xiulan Bao[1], Junsong Leng[2], Jincheng Mao[3*], Biyu Chen[1]

(1. *College of Engineering, Huazhong Agricultural University, Wuhan 430070, China*;
2. *School of Artificial Intelligence and Automation, Huazhong University of Science and Technology, Wuhan 430074, China*;
3. *School of Mechanical and Electrical Engineering, Wuhan Institute of Technology, Wuhan 430073, China*)

Abstract: The precise and automatic cutting of sheep carcasses can improve the quality of mutton. Robots are widely used in meat processing because of their good repeatability and high precision. Two essential problems encountered in robot working of sheep carcass processing are robot calibration and cutting trajectory planning. A method of cutting sheep carcasses based on 3D point clouds with a dual-robot system was proposed in this study. The dual-robot system consists of a 3D scanning system, a fixing device for sheep carcasses, and a cutting robot. The calibration of the dual-robot system was completed by solving the matrix problem ***AXB=YCZ*** using the iterative method and the closed-form method. The 3D model of a sheep carcass was constructed using a 3D scanner. The cutting scheme of the cutting robot was planned based on the processed 3D point clouds. To show the feasibility of the proposed sheep carcass processing scheme, practical experiments were carried out. The results of the experiments show that the cutting robot can accurately perform the cutting actions according to the planned cutting scheme. The system proposed in this study can improve the efficiency and precision of sheep carcass cutting.

Keywords: sheep carcass, trajectory planning, point cloud, dual-robot system, 3D
DOI: 10.25165/j.ijabe.20221505.7161

Citation: Bao X L, Leng J S, Mao J C, Chen B Y. Cutting of sheep carcass using 3D point cloud with dual-robot system. Int J Agric & Biol Eng, 2022; 15(5): 163–171.

1 Introduction

The consumption of meat products is increasing when the world's population is growing and people's eating habits are changing. Mutton is one of the meats that has seen the biggest increase in consumption. Because robots have the advantages of high flexibility and good repeatability, the application of robots in sheep carcass processing is one of the ways to improve the quality of mutton. The application of robots in sheep carcass processing is faced with many problems, such as the calibration of robot systems, sheep carcass positioning, and sheep carcass cutting trajectory planning.

Robots are widely used in agriculture[1,2], surgery[3], education[4], industry[5,6], and other fields. Robots have been widely used in the meat processing industry according to practical needs. Misimi et al.[7] developed a robot called Gribbot that is used to harvest the front half of chicken. It solves the problem of grasping and scraping chicken fillets from non-rigid chicken carcasses. Denmark designed a typical clean slaughter line. A series of robots cut the throat, loosen the fat end, divide the hind legs, open the carcass and perform evisceration. The application of these robots saves a great deal of labor[8]. Industrial Research Limited in Australia developed the world's first beef belly rip robot[9]. Singh et al.[10] developed a robotic brisket-cutting system for lamb and sheep carcass. The initial success rate of the system on lambs is 96% and on sheep is 95%. The application of the above robots in meat processing provides a lot of experience and help.

More and more cooperative dual-robot systems have been applied in the applications of rescue activity[11], aerial work[12], robotic surgery[13-15], payload transportation[16], and fruit harvest[17], among others. The dual-robot system has the advantage of large operating space and is suitable for sheep carcass processing. The application of a dual robot system must first solve the calibration problem. The calibration of a dual-robot system mainly involves flange-sensor, base-base, and flange-tool transformation matrices calibrations. Qiao et al.[18], Zhao et al.[19], Zhu et al.[20,21], Wang et al.[22] researched the calibration problem of a dual-robot system using step-by-step calibration methods. To reduce the calibration errors in step-by-step calibration methods. Yan et al.[23], Wu et al.[24], Wang et al.[25], Ma et al.[26] proposed several approaches for solving flange-sensor, base-base, and flange-tool transformation matrices calibrations problems simultaneously. The methods proposed by Yan et al. and Wu et al. had one common problem is that the iteration progress is time-consuming because it needs to carry out the least squares of all samples and calculate the inverse matrices in each iteration. The method proposed by Ma et al. can only be used in zero noise or small noise conditions. Wang et al.[27] proposed a closed-form method based on the Kronecker product and an iterative method to solve the dual-robot calibration problem, which converts a nonlinear problem into solving an optimization problem of a strictly convex function. This method has the advantages of high precision and high efficiency. In this study, the modified iterative method and the closed-form method were used to solve the dual-robot calibration problem.

Machine vision technologies are widely used in meat processing to solve problems of meat positioning and robot work trajectory planning. Mu et al.[28] designed a 3D vision-guided

Received date: 2021-11-03 **Accepted date:** 2022-03-16
Biographies: Xiulan Bao, PhD, Associate Professor, research interest: agricultural intelligent robot equipment, Email: orchidbaoxl@mail.hzau.edu.cn; **Junsong Leng**, MS, research interest: robot control and computer vision, Email: hzauljs@163.com; **Biyu Chen**, Master candidate, research interest: agricultural engineering, Email: chen__biyu@163.com.
***Corresponding author: Jincheng Mao**, PhD, Associate Professor, research interest: structural design and precision control for robots. School of Mechanical and Electrical Engineering, Wuhan Institute of Technology, Liufang Campus, No.206, Guanggu 1st Road, Donghu New & High Technology Development Zone, Wuhan 430070, China. Tel: +86-13871229154, Email: 14100304@wit.edu.cn.

system for half sheep carcass cutting robot. The images of the half-sheep carcass were obtained by the Azure Kinect camera, and the ribs and spine of the half-sheep carcass were identified using the Deeplab v3+ model. Bondø et al.[29] designed an automated salmonid slaughter line using machine vision. The stunned fish was scanned using 3D machine vision, the cut point was identified, and the bleed-cutting robot was used to cut the fish. Guire et al.[30] used structural light to extract the profile and key points of the spine of cattle carcasses. The robot then cuts the carcass along the characteristic lines between the key points. Cheng et al.[31] used Microsoft Kinect to develop a visual system for detecting insertion points on ovine carcasses. The image information was used to guide the cutter insert into the insertion point for cutting the belly of the ovine carcasses. Liu et al.[32] used the 2D camera to identify the porcine abdomen curve based on the grey step, and then the quintic spline curve is fitted from the image. Cong et al.[33] proposed a method of point cloud clustering combined with principal component analysis (PCA) to identify the cutting line position of the porcine abdomen. In the following study, Cong et al.[34] developed a porcine abdomen cutting robot system using binocular vision techniques based on kernel principal component analysis (KCPA). In summary, the technologies mentioned above have been applied to meat cutting successively, but different visual technologies bring different degrees of errors. Point cloud has great potential in planning the cutting trajectory of the sheep carcass because it can record the 3D features of the sheep carcass in the form of coordinates and vectors.

To achieve efficient and accurate cutting of sheep carcasses, a method of trajectory planning for cutting sheep carcasses based on 3D point clouds with the dual-robot system was innovatively proposed in this study. One of the contributions of this study is the design of a dual robot system for sheep carcass cutting. The closed-form method and iterative method were used to calibrate the dual-robot system. Another contribution of this study is to propose a cutting scheme based on the 3D point cloud of sheep carcasses. The feasibility of the scheme was verified by experiments.

2 Dual-robot system setup and calibration

2.1 System setup

As shown in Figure 1, the experimental devices consist of a 3D scanning system, a fixing device for sheep carcass, and a cutting robot. The sheep carcass is hung on the hanger using the hook. The cutting robot is directly opposite the scanning robot.

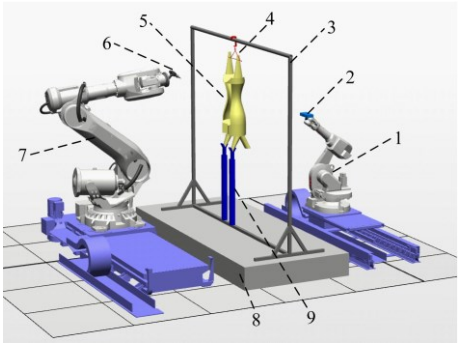

1. Scanning robot 2. 3D scanner 3. Hanger 4. Hook 5. Sheep carcass
6. Cutter 7. Cutting robot 8. Platform 9. Pneumatic clamps

Figure 1 Schematic diagram of the experimental scheme

2.1.1 3D scanning system

In this study, a 3D scanning system was used to construct the 3D model of the sheep carcass. As shown in Figure 2, the 3D scanning system consists of a 3D scanner (vision3d, China, PowersScan 2.3M 3D scanner, measurement accuracy ±0.015 mm, optimum measuring distance 640 mm), a scanning robot (ABB IRB 1600 10/1.45 robot, six DOFs, position repeatability 0.05 mm), a robot controller, and a computer (an Intel i7 9700 CPU with 3.00 GHz and an 8 GB DDR4 RAM, USA). The specific parameters of the scanning robot are shown in Table 1. The computer is connected to the scanning robot controller to plan the scanning trajectory of the scanning robot. The robot controller issues movement instructions to the scanning robot and the computer issues scanning instructions to the scanner.

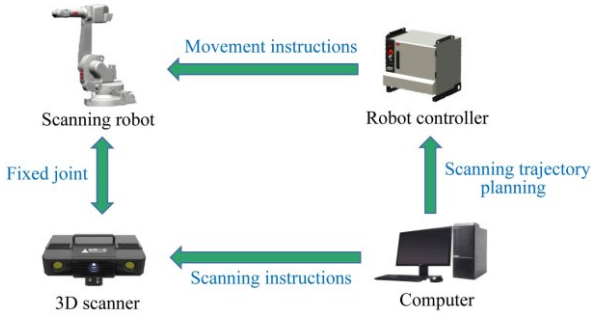

Figure 2 Schematic image of the 3D scanning system

2.1.2 Fixing device of sheep carcass

The fixing device was designed to solve the swinging problem of the sheep carcass that may occur during the scanning process. As shown in Figure 3, the fixing device of sheep carcass consists of a hanger, a hook, and two pneumatic clamps. The hanger is made of aluminum profiles (a length of 3 m, and a height of 2.5 m). One end of the hook is connected to the hanger, and the other end is connected to the hind legs of the sheep carcass. The two front legs of the sheep carcass are clamped by pneumatic clamps.

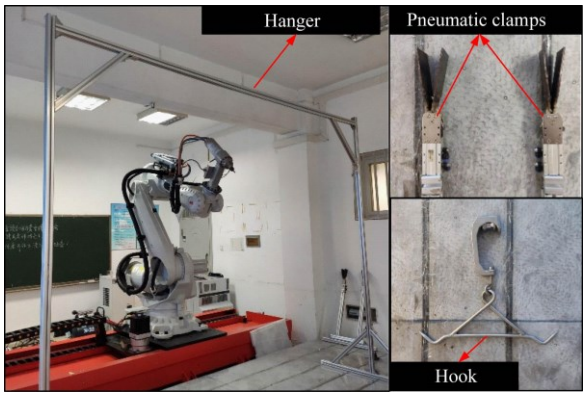

Figure 3 Fixing device of the sheep carcass

2.1.3 Cutting robot

The function of the cutting robot is to perform the cutting actions according to the planned cutting scheme. The model of the cutting robot is ABB IRB 6700-200/2.6 robot (six DOFs, position repeatability 0.05 mm). A cutter is mounted on the end-effector of the cutting robot. The cutting trajectory of the cutting robot is planned based on the 3D point clouds of sheep carcass. The parameters of the cutting robot are listed in Table 1.

2.2 System calibration

The cutting trajectory is planned according to the spatial coordinates of point clouds based on the basic coordinate system of the cutting robot. The spatial coordinates of the point clouds picked up by the 3D scanner are based on the scanner coordinate system. Therefore, the spatial coordinates transformation of point clouds among different coordinate systems is necessary. In this study, it is solved by finding the transformation matrices.

Table 1 Parameters of the dual-robot

Robot version	Reach/m	Payload/kg	Position repeatability/m	Path repeatability/mm	Working range	
IRB 1600-10/1.45	1.45	10	0.05	0.13	Axis 1	+180° to −180°
					Axis 2	+150° to −90°
					Axis 3	+65° to −245°
					Axis 4	+200° to −200°
					Axis 5	+115° to −115°
					Axis 6	+400° to −400°
IRB 6700-200/2.60	2.60	200	0.05	0.10	Axis 1	+170° to −170°
					Axis 2	+85° to −65°
					Axis 3	+70° to −180°
					Axis 4	+300° to −300°
					Axis 5	+130° to −130°
					Axis 6	+360° to −360°

2.2.1 Mathematical modeling of calibration problems

As shown in Figure 4, the calibration of the dual-robot system can be formulated into a matrix equation as $\boldsymbol{AXB}=\boldsymbol{YCZ}$. $\{\boldsymbol{O}_1\}$, $\{\boldsymbol{E}_1\}$, $\{\boldsymbol{S}\}$, $\{\boldsymbol{O}_2\}$, $\{\boldsymbol{E}_2\}$, and $\{\boldsymbol{T}\}$ represent the basic coordinate system of the scanning robot, the end-flange coordinate system of the scanning robot, the 3D scanner coordinate system, the basic coordinate system of the cutting robot, the end-flange coordinate system of the cutting robot, and the target coordinate system, respectively. Where $\boldsymbol{X}$, $\boldsymbol{Y}$, $\boldsymbol{Z}$ represent the unknown constant homogeneous transformation matrices from $\{\boldsymbol{E}_1\}$ to $\{\boldsymbol{S}\}$, from $\{\boldsymbol{O}_1\}$ to $\{\boldsymbol{O}_2\}$, and from $\{\boldsymbol{E}_2\}$ to $\{\boldsymbol{T}\}$, respectively. Symbols $\boldsymbol{A}$, $\boldsymbol{B}$, $\boldsymbol{C}$ represent the given varying homogeneous transformation matrices from $\{\boldsymbol{O}_1\}$ to $\{\boldsymbol{E}_1\}$, $\{\boldsymbol{S}\}$ to $\{\boldsymbol{T}\}$, and $\{\boldsymbol{O}_2\}$ to $\{\boldsymbol{E}_2\}$, respectively.

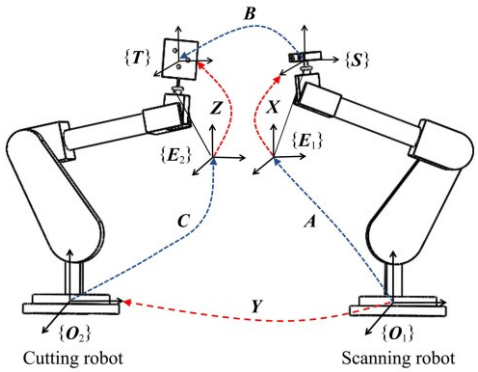

Note: $\{\boldsymbol{O}_1\}$, $\{\boldsymbol{E}_1\}$, $\{\boldsymbol{S}\}$, $\{\boldsymbol{O}_2\}$, $\{\boldsymbol{E}_2\}$, and $\{\boldsymbol{T}\}$ represent the basic coordinate system of the scanning robot, the end-flange coordinate system of the scanning robot, the 3D scanner coordinate system, the basic coordinate system of the cutting robot, the end-flange coordinate system of the cutting robot, and the target coordinate system, respectively. $\boldsymbol{X}$, $\boldsymbol{Y}$, and $\boldsymbol{Z}$ represent the unknown constant homogeneous transformation matrices from $\{\boldsymbol{E}_1\}$ to $\{\boldsymbol{S}\}$, from $\{\boldsymbol{O}_1\}$ to $\{\boldsymbol{O}_2\}$, and from $\{\boldsymbol{E}_2\}$ to $\{\boldsymbol{T}\}$, respectively. Symbols $\boldsymbol{A}$, $\boldsymbol{B}$, and $\boldsymbol{C}$ represent the given varying homogeneous transformation matrices from $\{\boldsymbol{O}_1\}$ to $\{\boldsymbol{E}_1\}$, $\{\boldsymbol{S}\}$ to $\{\boldsymbol{T}\}$, and $\{\boldsymbol{O}_2\}$ to $\{\boldsymbol{E}_2\}$, respectively.

Figure 4 Schematic diagram of calibration of the dual-robot system

It is obvious from Figure 4 that solving the matrix equation

$$\boldsymbol{AXB}=\boldsymbol{YCZ} \tag{1}$$

is the method for solving the calibration problem of the dual-robot system. A homogeneous transformation matrix $\boldsymbol{T}$ can be represented as

$$\boldsymbol{T}=\begin{bmatrix}\boldsymbol{R}_T & \boldsymbol{t}_T\\ \boldsymbol{0} & 1\end{bmatrix} \tag{2}$$

where, $\boldsymbol{R}_T$ represents a 3×3 rotation matrix and $\boldsymbol{t}_T$ represents a 3×1 translation vector. Equation (1) can be decomposed into the rotation and translation parts.

$$\boldsymbol{R}_A\boldsymbol{R}_X\boldsymbol{R}_B=\boldsymbol{R}_Y\boldsymbol{R}_C\boldsymbol{R}_Z \tag{3}$$

$$\boldsymbol{R}_A\boldsymbol{R}_X\boldsymbol{t}_B+\boldsymbol{R}_A\boldsymbol{t}_X+\boldsymbol{t}_A=\boldsymbol{R}_Y\boldsymbol{R}_C\boldsymbol{t}_Z+\boldsymbol{R}_Y\boldsymbol{t}_C+\boldsymbol{t}_Y \tag{4}$$

where, $\boldsymbol{R}_A$, $\boldsymbol{R}_X$, $\boldsymbol{R}_B$, $\boldsymbol{R}_Y$, $\boldsymbol{R}_C$, and $\boldsymbol{R}_Z$ are 3×3 rotation matrice of matrices A, X, B, Y, C, and Z, respectively. $\boldsymbol{t}_B$, $\boldsymbol{t}_X$, $\boldsymbol{t}_A$, $\boldsymbol{t}_Z$, $\boldsymbol{t}_C$, and $\boldsymbol{t}_Y$ are 3×1 translation vectors of matrices A, X, B, Y, C, and Z, respectively. Equation (3) is the rotation part and Equation (4) is the translation part. In the calibration process, the n sets of homogeneous transformation matrices $\boldsymbol{A}_i$, $\boldsymbol{B}_i$, and $\boldsymbol{C}_i$ (i=1, 2, 3, ..., n) were obtained by changing the attitudes of the two robots. Then, Equation (3) and Equation (4) can be extended to

$$\boldsymbol{R}_{A_i}\boldsymbol{R}_X\boldsymbol{R}_{B_i}=\boldsymbol{R}_Y\boldsymbol{R}_{C_i}\boldsymbol{R}_Z \tag{5}$$

$$\boldsymbol{R}_{A_i}\boldsymbol{R}_X\boldsymbol{t}_{B_i}+\boldsymbol{R}_{A_i}\boldsymbol{t}_X+\boldsymbol{t}_{A_i}=\boldsymbol{R}_Y\boldsymbol{R}_{C_i}\boldsymbol{t}_Z+\boldsymbol{R}_Y\boldsymbol{t}_{C_i}+\boldsymbol{t}_Y \tag{6}$$

where, $\boldsymbol{R}_{A_i}$, $\boldsymbol{R}_{B_i}$, $\boldsymbol{R}_{C_i}$, $\boldsymbol{t}_{A_i}$, $\boldsymbol{t}_{B_i}$, $\boldsymbol{t}_{C_i}$ (i=1, 2, 3, ..., n) represent rotation matrices and translation vectors of the ith group. Thus, solving Equation (1) is equivalent to solving Equations (5) and (6).

In this study, the modified iterative method is used to solve Equation (5). The closed-form method is used to solve Equation (6).

2.2.2 Iterative method

Solving for Equation (5) is equivalent to solving for the following objective function:

$$\begin{aligned}&\min g(\boldsymbol{R}_X,\boldsymbol{R}_Y,\boldsymbol{R}_Z)\\&=\frac{1}{n}\sum_{i=1}^{n}(\left\|\boldsymbol{R}_{A_i}\boldsymbol{R}_X\boldsymbol{R}_{B_i}-\boldsymbol{R}_Y\boldsymbol{R}_{C_i}\boldsymbol{R}_Z\right\|_F^2)\\&\text{s.t. }\boldsymbol{R}_X\boldsymbol{R}_X^T=\boldsymbol{I},\ \boldsymbol{R}_Y\boldsymbol{R}_Y^T=\boldsymbol{I},\ \boldsymbol{R}_Z\boldsymbol{R}_Z^T=\boldsymbol{I}\end{aligned} \tag{7}$$

where, ming() is the objective function, $\left\|\boldsymbol{R}_{A_i}\boldsymbol{R}_X\boldsymbol{R}_{B_i}-\boldsymbol{R}_Y\boldsymbol{R}_{C_i}\boldsymbol{R}_Z\right\|_F^2$ is the residual error item of Equation (5), F is the Frobenius norm, $\boldsymbol{I}$ is the orthogonal matrix. $\boldsymbol{R}_X$, $\boldsymbol{R}_Y$, $\boldsymbol{R}_z$ are orthogonal matrices. The Lagrangian relaxation method of Equation (8) is used to establish the objective function because it is difficult to find the optimal solution directly under the constraints of Equation (7). It converts the minimization problem with constraints to that without constraints.

$$\begin{aligned}&\min g(\boldsymbol{R}_X,\boldsymbol{R}_Y,\boldsymbol{R}_Z)\\&=\frac{1}{n}\sum_{i=1}^{n}(\mu_1\left\|\boldsymbol{R}_{A_i}\boldsymbol{R}_X\boldsymbol{R}_{B_i}-\boldsymbol{R}_Y\boldsymbol{R}_{C_i}\boldsymbol{R}_Z\right\|_F^2+\ldots\\&\mu_2\left\|\boldsymbol{R}_X\boldsymbol{R}_X^T-\boldsymbol{I}\right\|_F^2+\mu_3\left\|\boldsymbol{R}_Y\boldsymbol{R}_Y^T-\boldsymbol{I}\right\|_F^2+\mu_4\left\|\boldsymbol{R}_Z\boldsymbol{R}_Z^T-\boldsymbol{I}\right\|_F^2)\end{aligned} \tag{8}$$

where, $\left\|\boldsymbol{R}_X\boldsymbol{R}_X^T-\boldsymbol{I}\right\|_F^2$, $\left\|\boldsymbol{R}_Y\boldsymbol{R}_Y^T-\boldsymbol{I}\right\|_F^2$, and $\left\|\boldsymbol{R}_Z\boldsymbol{R}_Z^T-\boldsymbol{I}\right\|_F^2$ are penalty terms that force $\boldsymbol{R}_X$, $\boldsymbol{R}_Y$, and $\boldsymbol{R}_z$ to be orthogonal matrices. Symbols μ_1, μ_2, μ_3, μ_4 are weight coefficients. The application of the Lagrangian relaxation method makes the calculation faster. But the final solution of $\boldsymbol{R}_X$, $\boldsymbol{R}_Y$, and $\boldsymbol{R}_z$ may not satisfy the orthogonality strictly. Therefore, it is indispensable to make $\boldsymbol{R}_X$, $\boldsymbol{R}_Y$, and $\boldsymbol{R}_z$ strictly orthogonal by normalizing the solution. The

residual error items of Equation (8) can be defined as Equation (9) to simplify the expression.

$$\begin{aligned} \boldsymbol{E}_1 &= \boldsymbol{R}_{A_i}\boldsymbol{R}_X\boldsymbol{R}_{B_i} - \boldsymbol{R}_Y\boldsymbol{R}_{C_i}\boldsymbol{R}_Z \\ \boldsymbol{E}_2 &= \boldsymbol{R}_X\boldsymbol{R}_X^T - \boldsymbol{I}, \boldsymbol{E}_3 = \boldsymbol{R}_Y\boldsymbol{R}_Y^T - \boldsymbol{I}, \boldsymbol{E}_4 = \boldsymbol{R}_Z\boldsymbol{R}_Z^T - \boldsymbol{I} \end{aligned} \tag{9}$$

Substituting Equation (9) into Equation (8), the objective function can be rewritten as

$$\begin{aligned} &\min g(\boldsymbol{R}_X, \boldsymbol{R}_Y, \boldsymbol{R}_Z) \\ &= \frac{1}{n}\sum_{i=1}^{n}(\mu_1\|\boldsymbol{E}_1\|_F^2 + \mu_2\|\boldsymbol{E}_2\|_F^2 + \mu_3\|\boldsymbol{E}_3\|_F^2 + \mu_4\|\boldsymbol{E}_4\|_F^2) \\ &= \frac{1}{n}\sum_{i=1}^{n}(\mu_1 tr(\boldsymbol{E}_1^T\boldsymbol{E}_1) + \mu_2 tr(\boldsymbol{E}_2^T\boldsymbol{E}_2) + \mu_3 tr(\boldsymbol{E}_3^T\boldsymbol{E}_3) + \mu_4 tr(\boldsymbol{E}_4^T\boldsymbol{E}_4)) \\ &= \frac{1}{n}\sum_{i=1}^{n} g_i(\boldsymbol{R}_X, \boldsymbol{R}_Y, \boldsymbol{R}_Z) \end{aligned} \tag{10}$$

where, tr(•) represents the trace of a matrix. It is obvious that the Frobenius norm and the 2-norm are both strictly convex functions of their respective arguments. Therefore, the objective Equation (10), which is the sum of strictly convex functions, is still strictly convex. The problem of solving the matrix Equation (5) is converted to a strictly convex optimization problem of Equation (10).

In this study, the Gradient Descent (GD) algorithm was used to solve the optimization problem of the strict convex Equation (10). A typical iteration of GD for Equation (10) is represented as

$$\boldsymbol{V}_{t+1} = \boldsymbol{V}_t - \eta_t\nabla_{\boldsymbol{V}_t} g(\boldsymbol{V}_t) \tag{11}$$

where, $\boldsymbol{V}_t = [\boldsymbol{R}_{X_t}, \boldsymbol{R}_{Y_t}, \boldsymbol{R}_{Z_t}]$ represents the 3×9 independent variable matrix at the tth iteration, η_t (η_t>0) represents the step size, $\nabla_{\boldsymbol{V}_t} g(\boldsymbol{V}_t)$ represents the gradient of Equation (10) at $\boldsymbol{V}_t$. Stochastic Variance Reduced Gradient with Barzilai-Borwein (SVRG-BB) is derived from GD which has high computational efficiency and good iteration stability. The iteration step sizes η_t (η_t>0) and the expression of the gradient $\nabla_{\boldsymbol{V}_t} g(\boldsymbol{V}_t)$ are imperative to SVRG-BB. Appropriate selection of step size can improve the calculation efficiency and stability of iteration. SVRG-BB only applies the case where the independent variable is a scalar or a vector. But independent variable $\boldsymbol{V}_t$ is a 3×9 matrix in this article which means the expression of η_t in SVRG-BB is no longer applicable. The expression of η_t is modified as Equation (12) to solve the problem.

$$\eta_t = \|\boldsymbol{V}_t - \boldsymbol{V}_{t-1}\|_F^2 / \left\|(\boldsymbol{V}_t - \boldsymbol{V}_{t-1})^T(\nabla_{\boldsymbol{V}_t} g(\boldsymbol{V}_t) - \nabla_{t-1} g(\boldsymbol{V}_{t-1}))\right\|_F \tag{12}$$

According to the matrix derivation rule, the gradient $\nabla_V g(V)$ of the objective Equation (10) is derived as

$$\begin{aligned} \nabla_V g(V) &= \frac{\partial g(V)}{\delta V} = \left[\frac{\partial g(\boldsymbol{V})}{\delta \boldsymbol{R}_X}, \frac{\partial g(\boldsymbol{V})}{\delta \boldsymbol{R}_Y}, \frac{\partial g(\boldsymbol{V})}{\delta \boldsymbol{R}_Z}\right] = \frac{1}{n}\sum_{i=1}^{n}\nabla_{\boldsymbol{V}} g_i(\boldsymbol{V}) \\ &= \frac{2}{n}\sum_{i=1}^{n}\begin{bmatrix} [\mu_1(\boldsymbol{R}_X\boldsymbol{R}_{B_i}\boldsymbol{R}_{B_i}^T - \boldsymbol{R}_{A_i}^T\boldsymbol{R}_Y\boldsymbol{R}_{C_i}\boldsymbol{R}_Z\boldsymbol{R}_{B_i}^T) + 2\mu_3(\boldsymbol{R}_X\boldsymbol{R}_X^T\boldsymbol{R}_X - \boldsymbol{R}_X)], \\ [\mu_1(\boldsymbol{R}_Y\boldsymbol{R}_{C_i}\boldsymbol{R}_Z\boldsymbol{R}_Z^T\boldsymbol{R}_{C_i}^T - \boldsymbol{R}_{A_i}\boldsymbol{R}_X\boldsymbol{R}_{B_i}\boldsymbol{R}_Z^T\boldsymbol{R}_{C_i}^T) + 2\mu_4(\boldsymbol{R}_Y\boldsymbol{R}_Y^T\boldsymbol{R}_Y - \boldsymbol{R}_Y)], \\ [\mu_1(\boldsymbol{R}_{C_i}^T\boldsymbol{R}_Y^T\boldsymbol{R}_Y\boldsymbol{R}_{C_i}\boldsymbol{R}_Z - \boldsymbol{R}_{C_i}^T\boldsymbol{R}_Y^T\boldsymbol{R}_{A_i}\boldsymbol{R}_X\boldsymbol{R}_{B_i}) + 2\mu_5(\boldsymbol{R}_Z\boldsymbol{R}_Z^T\boldsymbol{R}_Z - \boldsymbol{R}_Z)], \end{bmatrix}_{3\times 9} \end{aligned} \tag{13}$$

2.2.3 Closed form method

Equation (4) can be rewritten as

$$\boldsymbol{P}\boldsymbol{t} = \boldsymbol{c} \tag{14}$$

where, $\boldsymbol{P} = [\boldsymbol{R}_A \quad -\boldsymbol{I} \quad -\boldsymbol{R}_Y \boldsymbol{R}_C]$, $\boldsymbol{t} = [\boldsymbol{t}_X^T \quad \boldsymbol{t}_Y^T \quad \boldsymbol{t}_Z^T]^T$, $\boldsymbol{c} = \boldsymbol{R}_Y\boldsymbol{t}_C - \boldsymbol{t}_A - \boldsymbol{R}_A\boldsymbol{R}_X\boldsymbol{t}_B$. For n groups of dual-robot attitudes. They can be represented as

$$\tilde{\boldsymbol{P}}\boldsymbol{t} \quad \tilde{\boldsymbol{c}} \tag{15}$$

where, $\tilde{\boldsymbol{P}} \quad \boldsymbol{J} \quad \boldsymbol{J}_2 \quad \ldots \quad \boldsymbol{J}_n]^T$, $\tilde{\boldsymbol{c}} \quad \boldsymbol{c} \quad \boldsymbol{c} \quad \ldots \quad \boldsymbol{c}_n]^T$. So the translational component $\boldsymbol{t}$ can be solved by Equation (16).

$$\boldsymbol{t} = (\tilde{\boldsymbol{J}}\ \tilde{\boldsymbol{J}} \quad \tilde{\boldsymbol{J}}\ \tilde{\boldsymbol{c}} \tag{16}$$

Equation (5) is still satisfied when any two of $\boldsymbol{R}_X$, $\boldsymbol{R}_Y$, and $\boldsymbol{R}_z$ multiply themselves by −1.

$$\begin{aligned} \boldsymbol{R}_{A_i}(-\boldsymbol{R}_X)\boldsymbol{R}_{B_i} &= (-\boldsymbol{R}_Y)\boldsymbol{R}_{C_i}\boldsymbol{R}_Z \\ \boldsymbol{R}_{A_i}(-\boldsymbol{R}_X)\boldsymbol{R}_{B_i} &= \boldsymbol{R}_Y\boldsymbol{R}_{C_i}(-\boldsymbol{R}_Z) \\ \boldsymbol{R}_{A_i}\boldsymbol{R}_X\boldsymbol{R}_{B_i} &= (-\boldsymbol{R}_Y)\boldsymbol{R}_{C_i}(-\boldsymbol{R}_Z) \end{aligned} \tag{17}$$

The translational components will be far from the true value when one of the situations in Equation (17) occurs. To solve this problem, the residual error e can be defined as

$$e = \| \boldsymbol{AXB} - \boldsymbol{YCZ} \|_F \tag{18}$$

where, $\|\bullet\|_F$ represents the Frobenius' norm of a matrix. Find the right combination by changing the sign of $\boldsymbol{R}_X$, $\boldsymbol{R}_Y$, and $\boldsymbol{R}_z$ which makes a minimum residual e. In other words, there are eight different symbol combinations of $\boldsymbol{R}_X$, $\boldsymbol{R}_Y$, and $\boldsymbol{R}_z$. Calculate the residual error of each combination and find the combination when the residual error is the minimum. In this way, the correct combination can be obtained. Then the translational components $\boldsymbol{t}$ can be calculated by Equation (16). The closed-form method ensures the accuracy of the results and the calculation speed is fast.

3 3D modeling and cutting scheme of sheep carcass

3.1 3D modeling of sheep carcass

Add the specific parameters of the cutter and the 3D scanner to the reachable space simulation of the dual-robot system. As shown in Figure 5, the reachable spaces of the two robots form an intersection which is the reachable space of the dual-robot system. As long as the sheep carcass is placed in the working reachable space of the dual-robot system, the 3D modeling of the sheep carcass can be realized.

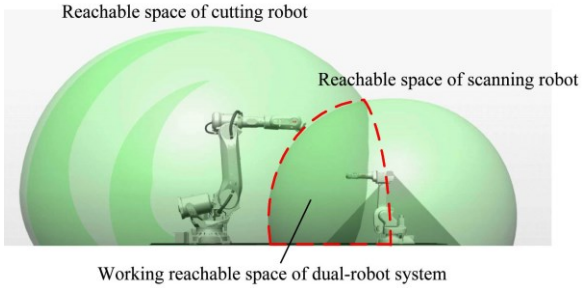

Figure 5 Working reachable space of dual-robot system

3D modeling of the sheep carcass is carried out after the experimental devices have been set up according to Figure 1. Picking up the 3D point clouds of the sheep carcass as much as possible is the key to the experiment. The scheme that the front of the scanning robot faces the back of the sheep carcass is adopted, which ensures the 3D point clouds of the back and two flanks of the sheep carcass can be picked up. It is acceptable not to scan the abdomen that has been cut open, as little useful surface information can be obtained from the abdomen.

After the sheep carcass has been hung up, a 3D model of the sheep carcass is constructed according to the flow in Figure 6. It starts by connecting the 3D scanner to the computer. Then adjust the attitude of the scanning robot and focus the 3D scanner on the surface of the sheep carcass. The spatial position of the 3D scanner is defined as the marked point. The attitude date of the scanning robot is recorded in the controller. This process is repeated dozens of times for the 3D scanner can as comprehensively as possible pick up the point clouds of the sheep carcass. Afterward, the scanning trajectory is planned according to the marked points so that the scanner can reach all the marked

points in turn for scanning. When the 3D scanner moves to a marked point, the scanning robot then maintains its attitude for 2 s. During this time, the 3D scanner completes the scan, and the point clouds are saved on the computer. The scanning of the sheep carcass is completed after the 3D scanner has scanned the carcass at the last marked point. It should be noted that the spatial coordinates of the point clouds are based on the 3D scanner coordinate system. So the spatial coordinates transformation of the point clouds is indispensable to realize the 3D modeling of sheep carcass based on the basic coordinate system of the cutting robot.

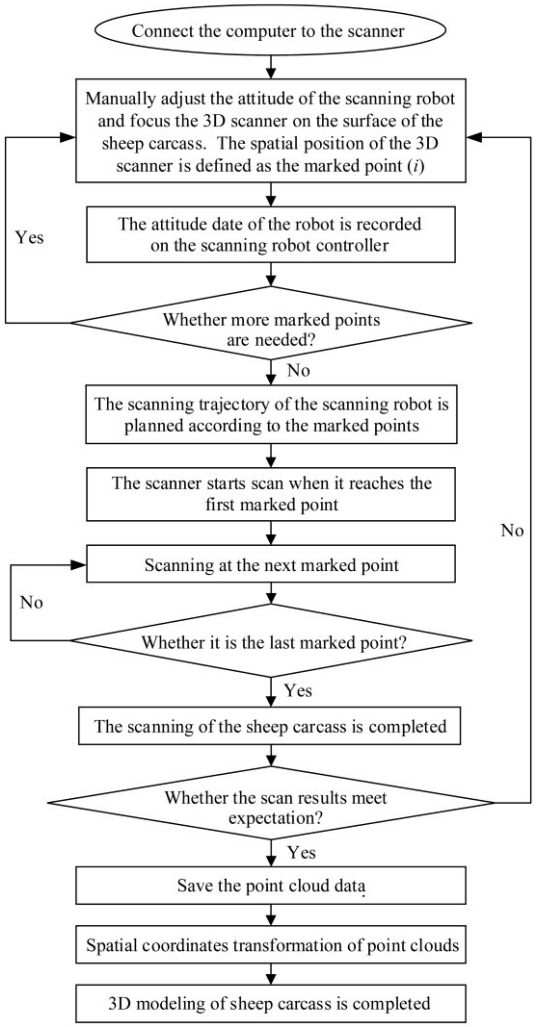

Figure 6 Flow of 3D modeling of sheep carcass

3.2 Cutting scheme of sheep carcass

To accurately segment each part of the sheep carcass. The cutting trajectory planning of the cutting robot is planned according to the Technical Specification for the Segmentation of Mutton NY/T 1564-2007, the agricultural industry standard issued by China in 2007[35]. As shown in Figure 7, the sheep carcass needs to be cut 7 times.

The 3D scanner scans the sheep carcass at n different marked points, and n groups of point clouds are picked up after the scanner has completed the scanning. $\boldsymbol{D}_i$ is a matrix containing the spatial coordinates of the ith group point clouds. Supposing there are m point clouds in the ith group. $\boldsymbol{D}_i$ is a $4\times m$ matrix that can be defined as

$$\boldsymbol{D}_i = \begin{bmatrix} a_1 & a_2 & \dots & a_m \\ b_1 & b_2 & \dots & b_m \\ c_1 & c_2 & \dots & c_m \\ 1 & 1 & 1 & 1 \end{bmatrix} \tag{19}$$

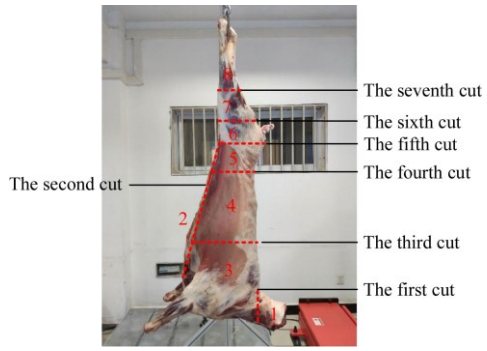

1. Neck 2. Breast and lap 3. Forequarter 4. Rack 5. Loin 6. Rump-bone on 7. Leg-chump on 8. Hind shank

Figure 7 Cutting scheme of experiment

The first three rows of each column of the matrix record the spatial coordinates of a point cloud in $\{\boldsymbol{S}\}$. To satisfy the matrix operation, the elements of the fourth row are set to 1. $\boldsymbol{Q}_i$ is a $4\times m$ matrix that contains the transformed spatial coordinates of the ith group of point clouds. It can be represented as

$$\boldsymbol{Q}_i = \boldsymbol{Y}^{-1}\boldsymbol{A}_i\boldsymbol{X}\boldsymbol{D}_i \tag{20}$$

where, $\boldsymbol{X}$ represents the constant homogeneous transformation matrix from $\{\boldsymbol{E}_1\}$ to $\{\boldsymbol{S}\}$. $\boldsymbol{Y}$ is the constant homogeneous transformation matrix from $\{\boldsymbol{O}_1\}$ to $\{\boldsymbol{O}_2\}$. $\boldsymbol{Y}^{-1}$ is the inverse matrix of $\boldsymbol{Y}$. $\boldsymbol{X}$ and $\boldsymbol{Y}$ are solved by Equation (10). $\boldsymbol{A}_i$ can be obtained from the scanning robot controller. For all of the spatial coordinates of the point clouds, there exists

$$\boldsymbol{Q} = [\boldsymbol{Q}_1 \quad \boldsymbol{Q}_2 \quad \dots \quad \boldsymbol{Q}_n] \tag{21}$$

where, the first three rows of matrix $\boldsymbol{Q}$ contain the transformed spatial coordinates of the point clouds. It means the spatial coordinates of the point clouds based on $\{\boldsymbol{O}_2\}$ are obtained after the spatial coordinates transformation has been completed. To accurately cut the sheep carcass, the cutter which is mounted on the end-effector of the cutting robot must reach the starting point of each cut. And then the sheep carcass was cut by the cutter. But before that, planning the cutting trajectory is indispensable.

Take the jth (j=1,2,3,4,5,6,7) cut for example. Firstly, The point clouds near the incisions are extracted, and then the trajectory planning of the cutting is planned according to the spatial coordinates of the point clouds. Because there are a lot of point clouds and they are too close to each other, the robot moves slowly and unsteadily from one point cloud to another. Therefore, sparse processing of point clouds is necessary. After that, inputting the spatial coordinates of the sparsely processed point clouds into the controller of the cutting robot, so that the cutter can reach the spatial position of the point clouds in turn.

4 Experiments results

4.1 Calibration of the dual-robot system

As shown in Figure 8, the devices of the calibration experiment consist of two robots, the 3D scanner, and the calibration target board. By randomly changing the attitudes of the two robots, the 3D scanner is used to scan the marker on the calibration target. The number of markers points is set as 3, and the 3D coordinates of the markers point in $\{\boldsymbol{S}\}$ are recorded with a matrix ($\boldsymbol{B}_i$). Repeating the process 50 times. $\boldsymbol{A}_i$ and $\boldsymbol{C}_i$ can be read separately from the scanning robot controller and the cutting robot controller. The practical experiment of the calibration of the dual-robot system is shown in Figure 9.

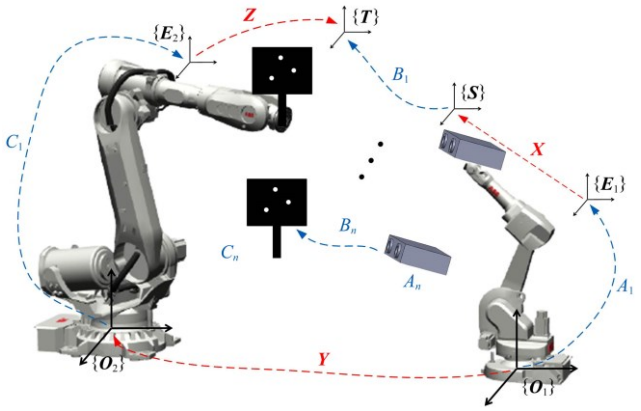

Note: A_i (i=1,… , n) is the pose data of the scanning robot. B_i (i=1,… , n) is the pose data of the cutting robot. C_i (i=1,… , n) is the 3D coordinates of the markers point in $\{S\}$.

Figure 8 Schematic diagram of calibration experiment

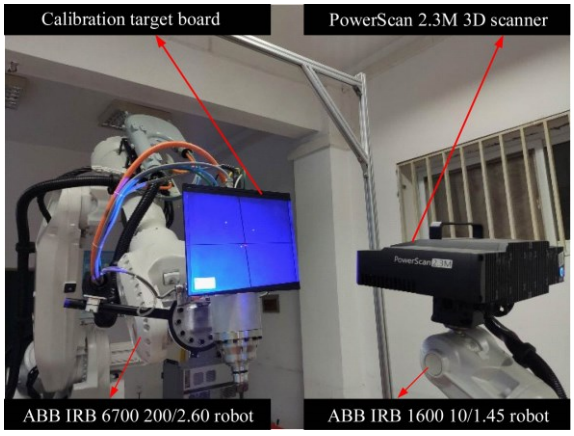

Figure 9 Practical experiment of calibration of dual-robot system

For the rotation parts. The algorithm flow of SVRG to Equation (10) is described in Figure 10, the weight coefficients μ_1, μ_2, μ_3, μ_4 were respectively set to 1, 1, 1, 1, the update frequency m was set to 3, and the initial step size η_0 was set to 0.1. The translation parts are obtained by using the closed-form method. The resulting matrices $\boldsymbol{X}$, $\boldsymbol{Y}$, and $\boldsymbol{Z}$ are as follows.

$$\boldsymbol{X}=\begin{bmatrix}\boldsymbol{R}_X & \boldsymbol{t}_X\\ \boldsymbol{0} & 1\end{bmatrix}=\begin{bmatrix}0.1321 & 0.9766 & -0.1145 & -36.7082\\ -0.9781 & 0.1428 & 0.0845 & -12.2293\\ 0.1001 & 0.1022 & 0.9810 & -2.8301\\ 0 & 0 & 0 & 1\end{bmatrix}$$

$$\boldsymbol{Y}=\begin{bmatrix}\boldsymbol{R}_Y & \boldsymbol{t}_Y\\ \boldsymbol{0} & 1\end{bmatrix}=\begin{bmatrix}-0.9974 & 0.0112 & 0.0060 & 3.1797\\ -0.0113 & -0.9970 & -0.0028 & 46.1410\\ 0.0063 & -0.0026 & 0.9974 & 93.9787\\ 0 & 0 & 0 & 1\end{bmatrix} \quad (22)$$

$$\boldsymbol{Z}=\begin{bmatrix}\boldsymbol{R}_Z & \boldsymbol{t}_Z\\ \boldsymbol{0} & 1\end{bmatrix}=\begin{bmatrix}-0.0362 & 0.0466 & 0.9750 & 9.1395\\ -0.1919 & -0.9570 & -0.0381 & 15.2117\\ 0.9571 & -0.1905 & 0.0448 & -9.0273\\ 0 & 0 & 0 & 1\end{bmatrix}$$

4.2 3D modeling experiment of sheep carcass

As shown in Figure 11, the scanning area of the sheep carcass is divided into five parts. Name them Area 1, Area 2, Area 3, Area 4, and Area 5. The point clouds of the sheep carcass are picked up by scanning each area with the 3D scanner. Each area was scanned from top to bottom 5 times with the 3D scanner. In total, 25 scans are required in this work.

The sheep in the experiment is a 6-month-old Small Tail Han sheep weighing 27.8 kg. The scanning experiment is shown in Figure 12. The 3D scanning system completes the scanning of the sheep carcass in less than 2 min.

As shown in Figure 13. There are 25 groups of 3D point clouds in $\{\boldsymbol{S}\}$. The 3D model of the sheep carcass in $\{\boldsymbol{O}_2\}$ is obtained after the spatial coordinates transformation of point clouds has been completed according to Equation (20). Figure 14 shows the different views of the 3D model of the sheep carcass.

4.3 Cutting trajectory planning

The cutting positions of 100 sheep carcasses were recorded and analyzed. As shown in Figure 15, the vertical distance between the cross section of the first cut and the top of the neck is about 20% of the vertical distance between the end of the foreleg and the top of the neck. The vertical distance between the cross section of the third cut and the end of the foreleg is 30% of the vertical distance between the end of the back leg and the end of the foreleg. Similarly, the fourth cut is 50%, the fifth cut is 60%, the sixth cut is 67%, and the seventh cut is 77%.

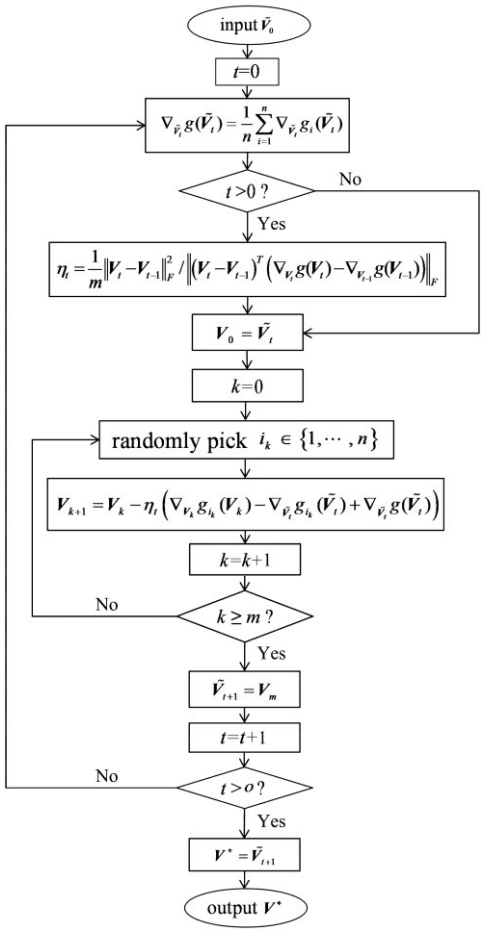

Note: $\tilde{V}$ is the initial value; n is the total number of groups of data; V_t is the independent variable matrix at the tth iteration; η_t is the iteration step size; m is the update frequency; o is the maximum number of iterations; V^* is the optimal value.

Figure 10 Algorithm flow of SVRG with a modified step size

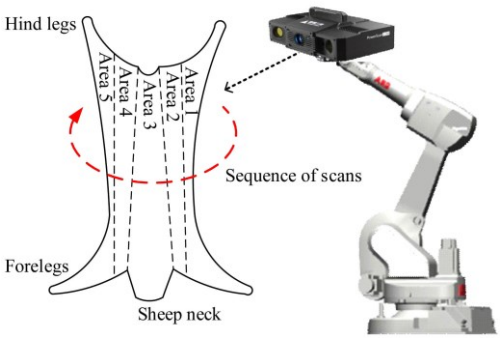

Figure 11 Scanning schematic diagram of sheep carcass 3D modeling

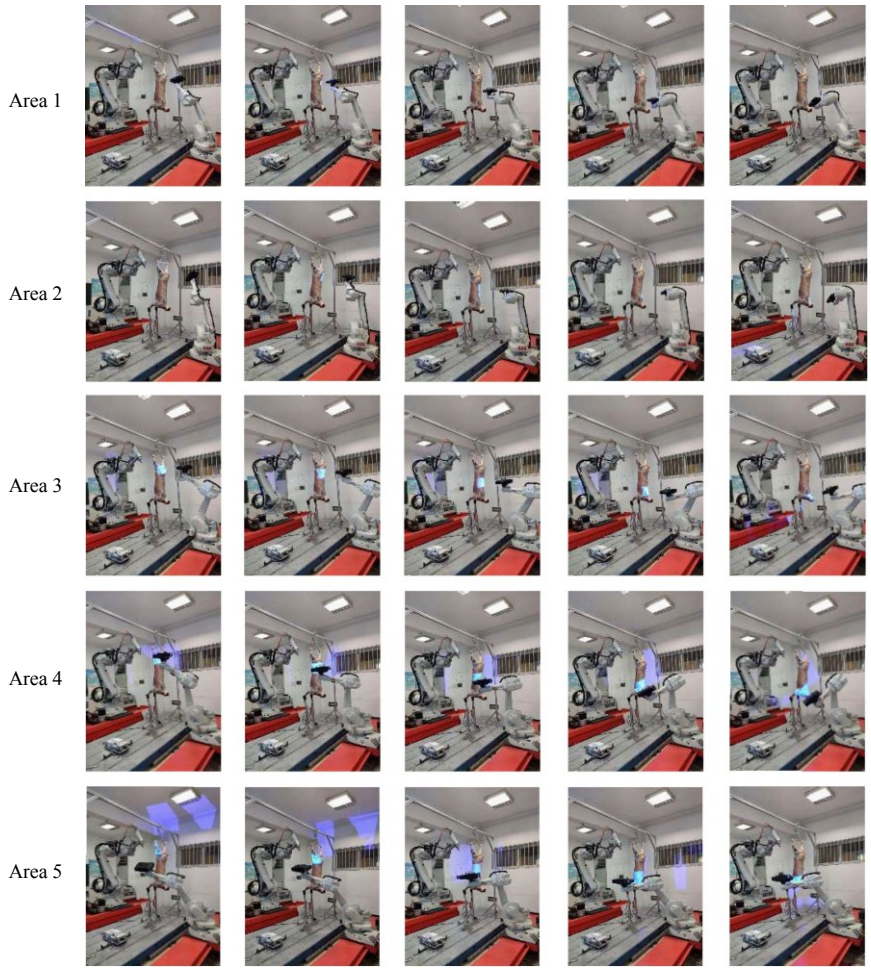

Figure 12 A total of twenty-five groups of point clouds are collected in the 3D scanning experiment of sheep carcass

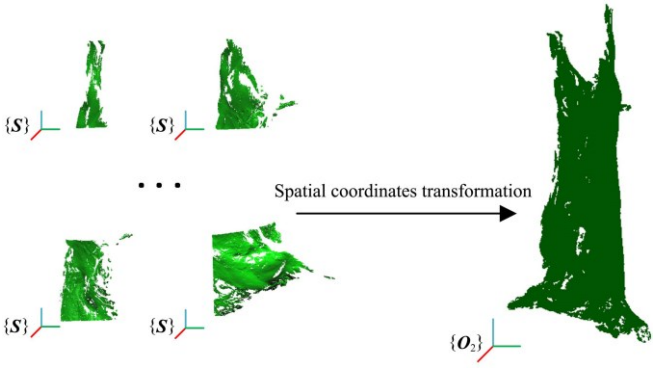

a. Distribution of point clouds of different groups in the {S} coordinate system b. 3D model of sheep carcass

Figure 13 Point cloud transformation and splicing

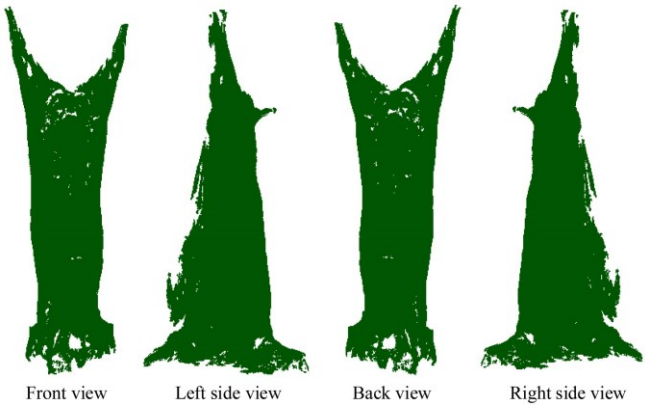

Figure 14 Different views of the 3D model of sheep carcass

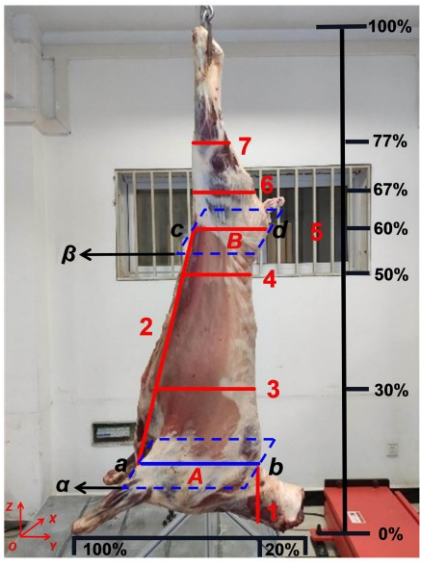

Figure 15 Position of each cut of sheep carcass

The second cut is determined by the first cut and the fifth cut. As shown in the figure. The *Z*-axis coordinate of plane α is the *Z*-axis coordinate of the starting point of the first cut. The point cloud of plane α is down-sampled to obtain a line (*ab*) parallel to the *Y*-axis. Similarly, plane β and line *cd* can also be obtained from the fifth cut. The line *ca* is the trajectory of the second cut.

As shown in Figure 16, the point clouds near the cuts are extracted according to the sheep carcass segmentation standards. There are hundreds of point clouds near each cut, which makes trajectory planning difficult for the following reasons: 1) The

workload is huge; 2) The point clouds are too dense.

Therefore, the downsampling was done for the point clouds. Although the number of point clouds has been significantly reduced, the main features of the cutting path are still preserved.

The cutting trajectory of the cutting robot was planned according to the spatial coordinates of processed point clouds. There are seven groups of data. Each group contains the spatial coordinates of the point clouds of each cut. Arrange the order among groups according to the order of each cut. The order of the point clouds in each group is arranged from the start point of the cut to the end.

As shown in Figure 17, the cutting robot performs the cutting actions according to the planned cutting trajectory. The cutting action of each cut is depicted by three pictures, including three cutting instantaneous states at the beginning of cutting, in cutting, and at the end of cutting. The experiment demonstrated that the cutting robot can accurately perform the cutting actions.

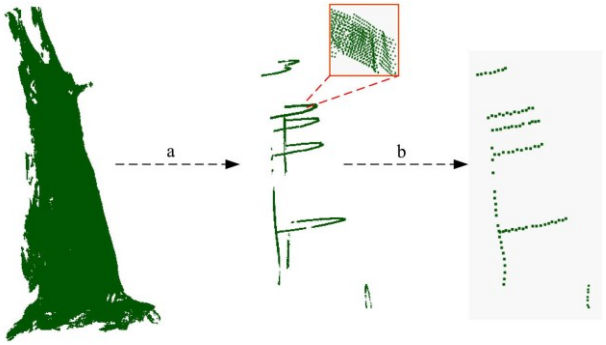

a. Point cloud extraction b. Point cloud downsampling

Figure 16 Point cloud extraction and point cloud downsampling

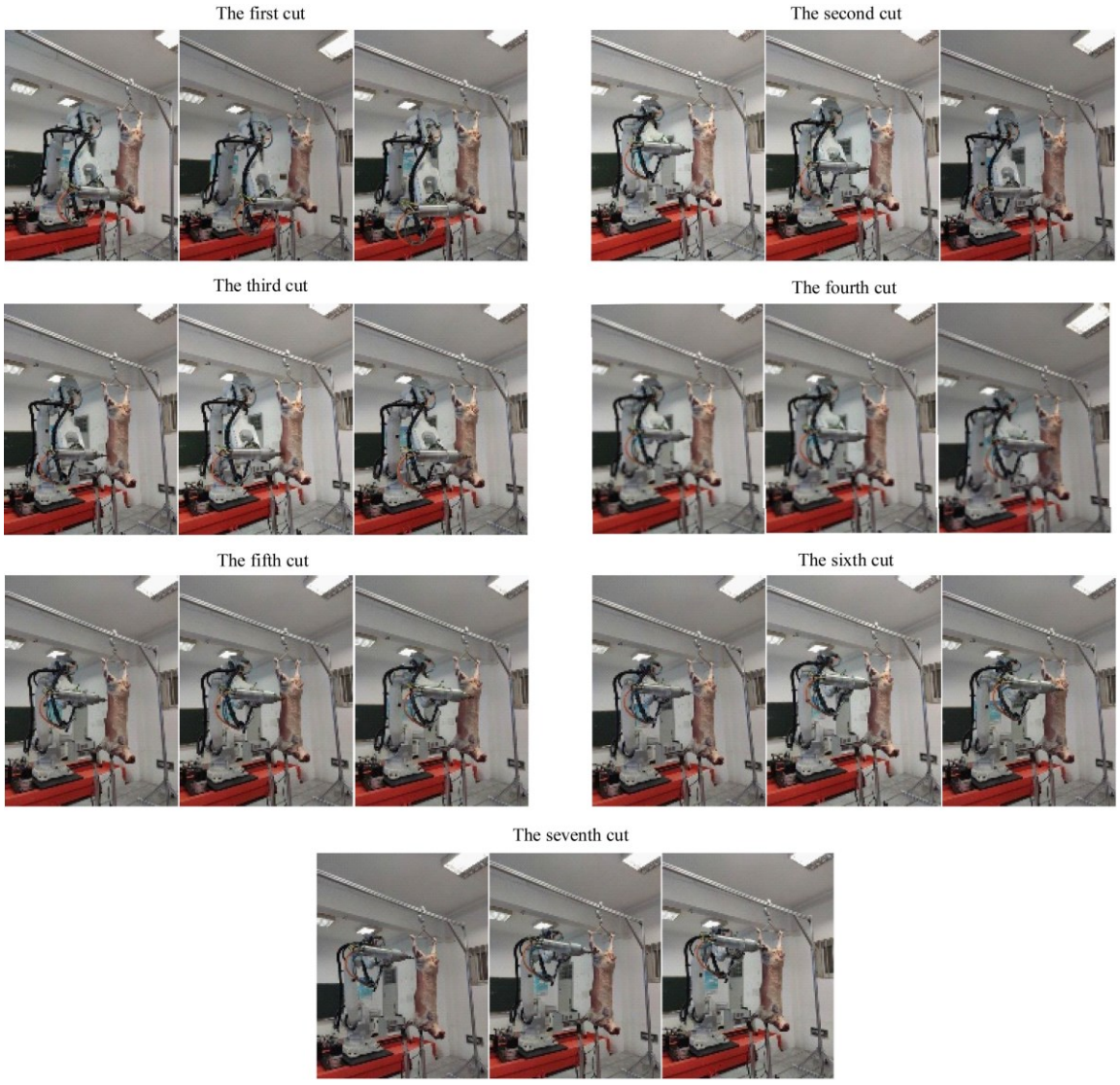

Figure 17 Cutting robot performs the cutting action according to the planned cutting trajectory

5 Conclusions

In this study, a dual-robot system was proposed to plan the cutting scheme of sheep carcass according to 3D point cloud spatial coordinates. The point clouds of the sheep carcass were obtained using a 3D scanner mounted on the end-effector of the scanning robot. The calibration of the dual-robot system was formulated into a matrix equation as $\boldsymbol{AXB=YCZ}$. The matrix was solved by the iterative method and the closed-form method. The 3D model of the sheep carcass based on the basic coordinate system of the cutting robot was obtained after the spatial coordinates of the point clouds have been transformed. The point clouds near the cut were extracted from the 3D model of the sheep carcass and down-sampled. According to the spatial coordinates of the processed point clouds, the cutting trajectory of the cutting robot for the sheep carcass was planned. To demonstrate the feasibility of the proposed scheme, a series of practical experiments were

carried out, including a dual-robot calibration experiment, a 3D scanning experiment of sheep carcass, and a cutting trajectory planning experiment. The experiments show that the cutting robot can perform the cutting actions accurately according to the planned cutting trajectory. This scheme can not only be applied to the automatic cutting of sheep carcass but also can be used as a reference for other poultry carcass-cutting schemes.

Acknowledgements

This work was financially supported by the Natural Science Foundation of Hubei Province, China (Grant No. 2021CFB 471) and the National Key Research and Development Program of China (Grant No. 2020YFD1000105-04).

[References]

[1] Williams H A, Jones M H, Nejati M, Seabright M J, Bell J, Penhall N D, et al. Robotic kiwifruit harvesting using machine vision, convolutional neural networks, and robotic arms. Biosystems Engineering, 2019; 181: 140–156.

[2] Zhao D A, Lyu J, Ji W, Zhang Y, Chen Y. Design and control of an apple harvesting robot. Biosystems Engineering, 2011; 110(2): 112–122.

[3] Du Z J, Liang Y L, Yan Z Y, Sun L N, Chen W. Human-robot interaction control of a haptic master manipulator used in laparoscopic minimally invasive surgical robot system. Mechanism and Machine Theory, 2021; 156: 104132. doi: 10.1016/j.mechmachtheory.2020.104132.

[4] Benedict J, Briggs H C. Application of robots in middle school math classes. In: Session: Advances in Aerospace Education I, AIAA, 2019; 2019-0070. doi: 10.2514/6.2019-0070.

[5] Möller C, Schmidt H C, Koch P, Böhlmann C, Kothe S M, Wollnack J, et al. Machining of large scaled CFRP-Parts with mobile CNC-based robotic system in aerospace industry. Procedia manufacturing, 2017; 14: 17–29.

[6] Wang G, Li W L, Jiang C, Zhu D H, Li Z W, Xu W, et al. Trajectory planning and optimization for robotic machining based on measured point cloud. IEEE Transactions on Robotics, 2021; 38(3): 1621–1637.

[7] Misimi E, Øye E R, Eilertsen A, Mathiassen J R, Åsebø O B, Gjerstad T, et al. GRIBBOT-Robotic 3D vision-guided harvesting of chicken fillets. Computers and Electronics in Agriculture, 2016; 121: 84–100.

[8] Hinrichsen L. Manufacturing technology in the Danish pig slaughter industry. Meat Science, 2010; 84(2): 271–275.

[9] Templer R, Osborn A, Nanu A, Blenkinsopp K, Friedrich W. Innovative robotic applications for beef processing. In: Proceedings of Australasian Conference on Robotics and Automation, 2002, Auckland: ARAA, 2002; pp.43–47.

[10] Singh J, Potgieter J, Xu W L. Ovine automation: robotic brisket cutting. Industrial Robot: An International Journal, 2012; 39(2): 191–196.

[11] Park D I, Kim H, Park C, Kim D. Design and analysis of the dual arm manipulator for rescue robot. In: 2017 IEEE International Conference on Advanced Intelligent Mechatronics (AIM), Munich: IEEE, 2017; pp.608–612. doi: 10.1109/AIM.2017.8014084.

[12] Lippiello V, Fontanelli G A, Ruggiero F. Image-based visual-impedance control of a dual-arm aerial manipulator. IEEE Robotics and Automation, 2018; 3(3): 1856–1863.

[13] Lehman A C, Berg K A, Dumpert J, Wood N A, Visty A Q, Rentschler M E, et al. Surgery with cooperative robots. Computer Aided Surgery, 2008; 13(2): 95–105.

[14] Wang J L, Ren H L, Meng M Q-H. A preliminary study on surgical instrument tracking based on multiple modules of monocular pose estimation. In: The 4th Annual IEEE International Conference on Cyber Technology in Automation, Control and Intelligent, Hong Kong: IEEE, 2014; pp.146–151. doi: 10.1109/CYBER.2014.6917451.

[15] Wu Q, Li M, Qi X, Hu Y, Li B, Zhang J. Coordinated control of a dual-arm robot for surgical instrument sorting tasks. Robotics and Autonomous Systems, 2018; 112(2019): 1–12.

[16] Bai H, Wen J T. Cooperative load transport: A formation-control perspective. IEEE Transactions on Robotics, 2010; 26(4): 742–750.

[17] Ling X, Zhao Y, Gong L, Liu C, Wang T. Dual-arm cooperation and implementing for robotic harvesting tomato using binocular vision. Robotics and Autonomous Systems, 2019; 114: 134–143.

[18] Qiao Y, Chen Y, Chen B, Xie J. A novel calibration method for multi-robots system utilizing calibration model without nominal kinematic parameters. Precision Engineering, 2017; 50: 211–221.

[19] Zhao D, Bi Y, Ke Y. Kinematic modeling and base frame calibration of a dual-machine-based drilling and riveting system for aircraft panel assembly. The International Journal of Advanced Manufacturing Technology, 2017; 94(5–8): 1873–1884.

[20] Zhu Q, Xie X, Li C, Xia G, Liu Q. Kinematic self-calibration method for dual-manipulators based on optical axis constraint. IEEE Access, 2019; 7: 7768–7782.

[21] Zhu Q, Xie X, Li C. Dual manipulator system calibration based on virtual constraints. Bulletin of the Polish Academy of Sciences-Technical Sciences, 2019; 67(6): 1149–1158.

[22] Wang J, Wang W, Wu C, Chen S L, Fu J, Lu G. A plane projection-based method for base frame calibration of cooperative manipulators. IEEE Transactions on Industrial Informatics, 2018; 15(3): 1688–1697.

[23] Yan S J, Ong S K, Nee A Y C. Registration of a hybrid robot using the Degradation-Kronecker method and a purely nonlinear method. Robotica, 2015; 34(12): 2729–2740.

[24] Wu L, Wang J L, Qi L, Wu K Y, Ren H L, Meng M Q-H. Simultaneous hand-eye, tool-flange, and robot-robot calibration for comanipulation by solving the ***AXB=YCZ*** problem. IEEE Transactions on Robotics, 2016; 32(2): 413–428.

[25] Wang J, Wu L, Meng M Q-H, Ren H. Towards simultaneous coordinate calibrations for cooperative multiple robots. In: 2014 IEEE/RSJ International Conference on Intelligent Robots and Systems, Chicago: IEEE, 2014; pp.410–415. doi: 10.1109/IROS.2014.6942592.

[26] Ma Q, Goh Z, Ruan S, Chirikjian G S. Probabilistic approaches to the ***AXB=YCZ*** calibration problem in multi-robot systems. Autonomous Robots, 2018; 42(7): 1497–1520.

[27] Wang G, Li W L, Jiang C, Zhu D H, Xie H, Liu X J, et al. Simultaneous calibration of multicoordinates for a dual-robot system by solving the ***AXB=YCZ*** problem. IEEE Transactions on Robotics, 2021; 37(4): 1172–1185.

[28] Mu S, Qin H B, Wei J, Wen Q K, Liu S H, Wang S C, et al. Robotic 3D vision-guided system for half-sheep cutting robot. Mathematical Problems in Engineering, 2020; 2020(Pt.35): 1520686. doi: 10.1155/2020/1520686.

[29] Bondø M S, Mathiassen J R, Vebenstad P A, Misimi E, Bar E M S, Toldnes B, et al. An automated salmonid slaughter line using machine vision. Industrial Robot: An International Journal, 2011; 38(4): 399–405.

[30] Guire G, Sabourin L, Gogu G, Lemoine E. Robotic cell for beef carcass primal cutting and pork ham boning in meat industry. Industrial Robot: An International Journal, 2010; 37(6): 532–541.

[31] Cheng D, Wong C K, Lim P P K. Vision system for the automation of ovine carcass processing. In: Proceedings of Australasian Conference on Robotics and Automation, Melbourne: The University of Melbourne, 2014; Paper No. 110.

[32] Liu Y, Cong M, Zheng H D, Liu D. Porcine automation: Robotic abdomen cutting trajectory planning using machine vision techniques based on global optimization algorithm. Computers and Electronics in Agriculture, 2017; 143: 193–200.

[33] Cong M, Wang Y H, Du Y, Liu D. Porcine abdomen cutting method using robot based on point cloud clustering and PCA. Journal of Huazhong University of Science and Technology (Natural Science Edition), 2020; 11: 54–59. (in Chinese)

[34] Cong M, Zhang J Q, Du Y, Wang Y H, Yu X, Liu D. A porcine abdomen cutting robot system using binocular vision techniques based on kernel principal component analysis. Journal of Intelligent & Robotic Systems, 2021; 101(4): 1–10.

[35] NY/T 1564-2007. Cutting technical specification of mutton, 2007. (in Chinese)